ACS NANO

www.acsnano.org

ARTICLE

Molecular Sensitizer-Loaded Monolayer Organic Semiconductors for High-Performance H_2S Sensors

Jianhang Guo,[▽] Jong Won Baek,[▽] Yeonghun Kang,[▽] Dongyoung Kim,[▽] Chungseong Park, Junhee Woo, Taoyu Zou, Euichul Shin, Qijing Wang, Yong-Young Noh, Steve Park, Jihan Kim,* Yun Li,* Il-Doo Kim,* and Kibum Kang*

Cite This: *ACS Nano* 2025, 19, 16175−16187

Read Online

ACCESS | Metrics & More | Article Recommendations | Supporting Information

ABSTRACT: **Monolayer organic semiconductors offer high gas sensitivity due to their exposed active channels and absence of grain boundaries, allowing them to interact directly with the analytes. However, such single-component organic sensors are typically lacking in selective adsorption sites, leading to practical hindrances such as limited chemical selectivity and slow recovery. In this study, we demonstrate a highly crystalline monolayer C_{10}-DNTT semiconductor film sensitized with F_4-TCNQ (F_4-TCNQ/C_{10}-DNTT), fabricated using a one-step solution-shearing codeposition method, which overcomes the aforementioned challenges to serve as a high-performance chemical gas sensor. Compared to pristine C_{10}-DNTT, the monolayer F_4-TCNQ/C_{10}-DNTT films showed an enhanced response to hydrogen sulfide (H_2S), an industrial pollutant and an important biomarker for respiratory disorders, as the sensitizer molecules promoted electronic interactions at the gas-organic semiconductor interface. Specifically, this resulted in a 5.3-fold increase in sensitivity to 5 ppm of H_2S, with high selectivity and improved recovery compared to pristine C_{10}-DNTT sensors. The precisely defined two-dimensional (2D) structure of the F_4-TCNQ/C_{10}-DNTT films enabled the investigation of layer-dependent sensing characteristics, reinforcing the significance of the monolayer configuration for achieving highly sensitive and selective H_2S sensing. This research provides an effective strategy for designing high-performance organic sensing devices and highlights the importance of layer precision in sensor response, contributing to the development of more efficient and reliable organic chemical sensors in the future.**

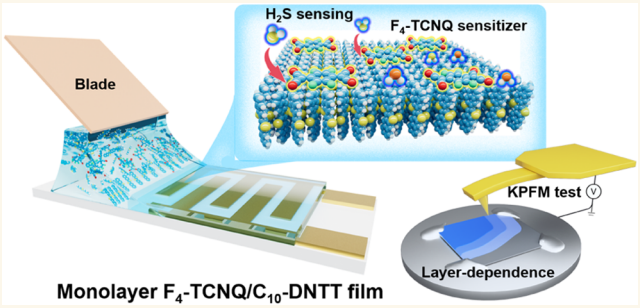

KEYWORDS: *molecular sensitizer, monolayer organic semiconductor, layer-dependence, toxic gas, chemical sensor*

The growing demand for wearable and portable devices has generated significant interest in organic electronic materials due to their high tunability, mechanical flexibility, and facile solution processability, making them competitive candidates for next-generation electronic applications.[1−3] In particular, semiconductor-based gas sensing devices for autonomous, on-site detection of trace analytes are essential for intelligent systems and the emerging Internet of Things (IoT) applications and could immediately benefit from the use of organic semiconductors over conventional semiconductors. Compared to inorganic semiconductors with broad, indiscriminate surface interaction with multiple different analytes, organic semiconductors have the competitive advantage in that they can be chemically tailored for selective detection of specific analytes even at room temperature while retaining adequate levels of sensitivity.[4] Thus, in recent years, tremendous efforts have been dedicated to enhancing the sensing performance of organic semiconductors, mainly through improving the surface adsorption of analytes and charge transfer capabilities. Reported strategies include engineering the morphologies with a high surface-to-volume ratio, employing heterostructures, and incorporating sensitizers.[5−9] Despite significant progress in organic semiconductor materials for gas sensing, however, challenges such as fabricating high-quality organic films still impede their practical

Received: March 20, 2025
Revised: April 10, 2025
Accepted: April 11, 2025
Published: April 16, 2025

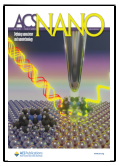

https://doi.org/10.1021/acsnano.5c04783
ACS Nano 2025, 19, 16175−16187

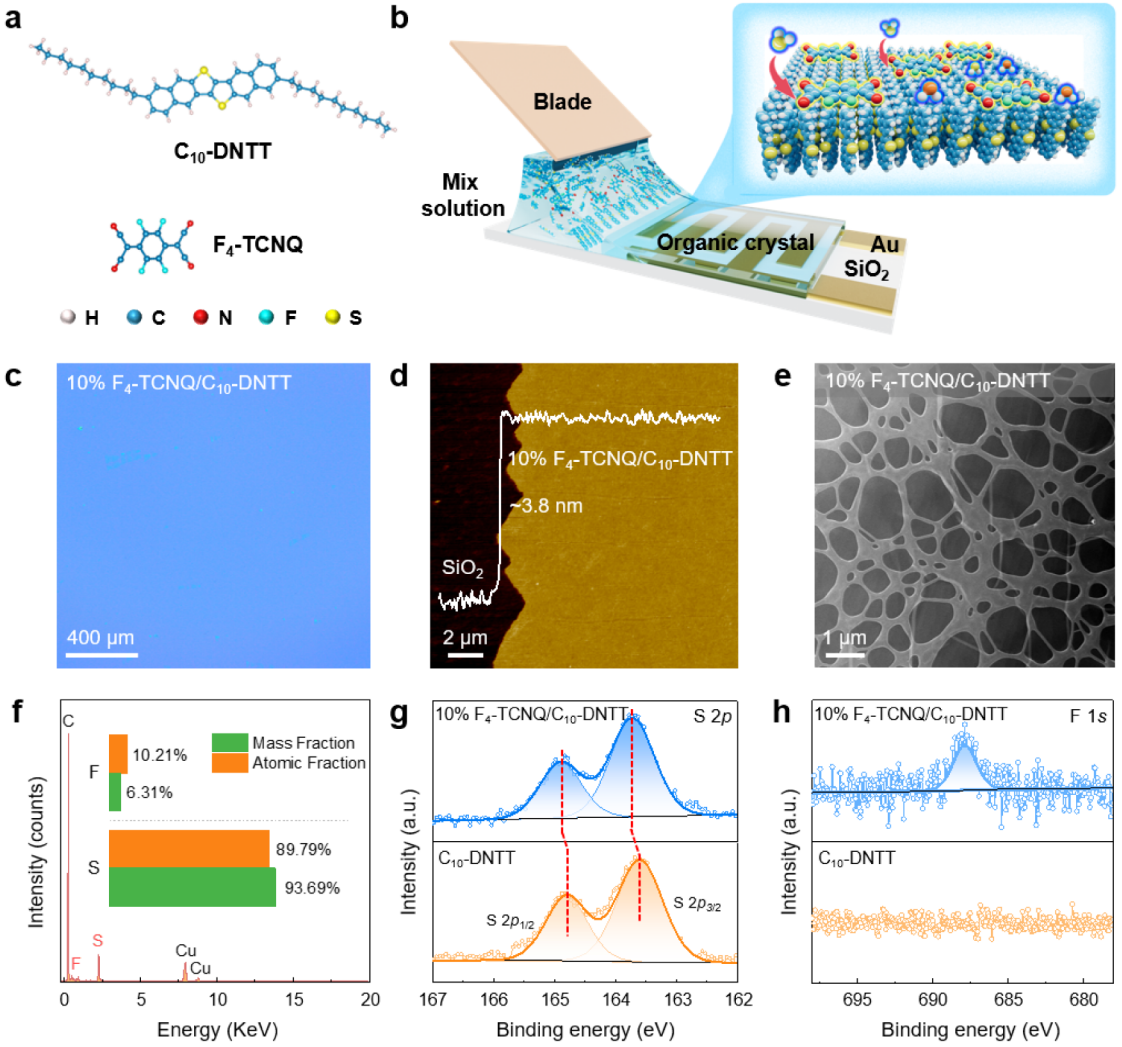

Figure 1. Fabrication and characterizations of monolayer 10% F_4-TCNQ/C_{10}-DNTT film. (a) Molecular structures of C_{10}-DNTT and F_4-TCNQ molecules. (b) Schematic of solution-sheared monolayer 10% F_4-TCNQ/C_{10}-DNTT on SiO_2 substrate with patterned Au IDEs. (c) OM image of the monolayer 10% F_4-TCNQ/C_{10}-DNTT on SiO_2 substrate. (d) AFM surface morphology image of the monolayer 10% F_4-TCNQ/C_{10}-DNTT on SiO_2 substrate. (e) TEM image of the monolayer 10% F_4-TCNQ/C_{10}-DNTT on a copper TEM grid and (f) corresponding EDS spectrum, the inset shows the mass fraction and the atomic fraction of sulfur and fluorine. XPS narrow scan spectra of (g) S 2*p* and (h) F 1*s* of pristine C_{10}-DNTT and monolayer 10% F_4-TCNQ/C_{10}-DNTT.

applications. Mainly, the diffusion of gas analytes into defect sites, such as grain boundaries, creates trapping or scattering centers for charge carriers within the organic sensing layer and results in sensor instability and irreversibility due to destructive gas-semiconductor interactions.[10] Moreover, as the gas analytes diffuse into the organic semiconductors in a vertical direction to the interface, they disrupt the conductive channels and limit the sensitivity of the device. This effect is particularly detrimental for structures with numerous interfacial defects or conventional bulk organic crystals. Therefore, rationally modulating the chemical interactions between the gas analytes and sensing materials, as well as facilitating interfacial charge transport, is crucial to improving gas sensitivity and selectivity. In this sense, a fundamentally different approach is necessary to successfully design high-performance organic semiconductor-based gas sensors.

To that end, two-dimensional (2D) organic semiconductors governed by van der Waals interactions present a unique opportunity to directly explore their structure−property relationship and offer valuable insights for designing advanced devices due to their precisely defined number of layers, long-range molecular order, and reduced grain boundary density.[11−15] A monolayer organic semiconductor that is directly exposed to the environment should offer high sensitivity to external stimuli, making it ideal for developing highly sensitive sensors capable of detecting minute environmental changes.[16−19] Moreover, scaling down the active semiconducting layer to a monolayer confines charge transport within a single conductive channel, eliminating the gas molecule diffusion bottleneck and enabling high-performance sensor devices.[20,21] Previous studies have demonstrated that monolayer organic semiconductor-based sensors indeed exhibit superior gas sensing performances compared to their bulk counterparts.[22,23] However, these single-component organic sensors faced persistent challenges, including low recovery and limited chemical selectivity due to the lack of selective adsorption sites. Additionally, the direct preparation of sensitized monolayer organic semiconductors through a bottom-up assembly process is rarely reported despite its importance for precisely incorporating functional moieties that

https://doi.org/10.1021/acsnano.5c04783
ACS Nano 2025, 19, 16175−16187

enhance selectivity and sensitivity. These challenges emphasize the urgent need for different materials engineering strategies to improve overall gas sensing performance, including recovery efficiency and chemical selectivity.

In this study, we present a one-step solution-shearing codeposition method to prepare a monolayer of molecular sensitizer-loaded organic semiconductor on the target substrate by mixing the active sensing material 2,9-didecyldinaphtho-[2,3-b:2′,3′-f]thieno[3,2-*b*]thiophene (C_{10}-DNTT) and the molecular sensitizer 2,3,5,6-tetrafluoro-7,7,8,8-tetracyanoquinodimethane (F_4-TCNQ) in specific volume ratios (denoted as x%-F_4-TCNQ/C_{10}-DNTT). The chemical composition and crystallinity characterizations showed that this approach can maintain the high crystalline nature of monolayer C_{10}-DNTT and confirmed the successful preparation of the sensitizer-loaded monolayer organic semiconductor sensor. Benefiting from the excellent electronic sensitization effect of F_4-TCNQ molecules on the sensing layer, the hydrogen sulfide (H_2S) gas sensing response of the 10% F_4-TCNQ-loaded C_{10}-DNTT (10% F_4-TCNQ/C_{10}-DNTT) was 5.3-fold higher than that of the pristine C_{10}-DNTT sensors. Our sensors also exhibit a sensing capability suitable for monitoring H_2S under high humidity conditions, which is not only a marker for industrial production such as petrochemicals and wastewater treatment, but also an important biomarker of the respiratory system like halitosis and chronic obstructive pulmonary disease, and has great potential for practical applications. Furthermore, the layer-dependent characteristics emphasized the importance of monolayer nanostructure in gas sensing devices due to the direct gas-semiconductor interactions with no additional delay from gas diffusion. Therefore, our findings establish a foundation for designing high-sensitivity organic chemical sensors for future gas sensing applications and suggest that this promising sensor design strategy may be applicable to other monolayer organic semiconductor films with compatible electronic properties and molecular structures.

RESULTS AND DISCUSSION

Figure 1 provides a schematic illustration of our high-performance organic semiconductor-based chemical sensor design. In Figure 1a, the p-type organic semiconductor C_{10}-DNTT with high carrier mobility was chosen as the active sensing material, and F_4-TCNQ with strong electron-withdrawing properties was selected as the molecular sensitizer. As shown schematically in Figure 1b, the sensor was fabricated by depositing the F_4-TCNQ-sensitized C_{10}-DNTT monolayer films as the sensing layer on a prefabricated SiO_2 substrate patterned with a pair of Au interdigitated electrodes (IDEs). The home-built solution-shearing setup was employed for organic film deposition, in which the organic solution was sandwiched between a blade and the target substrate. As the blade drags the solution, organic crystals are deposited near the meniscus formed between the blade's edge and the substrate, a process attributed to the self-assembly of organic molecules driven by intramolecular van der Waals interactions between adjacent molecules.[24] By optimizing the growth parameters, including substrate temperature and shearing speed, C_{10}-DNTT films can be deposited as a monolayer. As shown in Figure S1, millimeter-sized high crystalline C_{10}-DNTT films with a thickness of ∼3.8 nm can be deposited on the SiO_2 substrate, consistent with the thickness of the crystallographic *c*-axis of monolayer C_{10}-DNTT.[25] The F_4-TCNQ-sensitized C_{10}-DNTT films were prepared using a solution-shearing codeposition method,[26] in which the solution consisted of C_{10}-DNTT and F_4-TCNQ anisole solution with the equal mass concentration mixed in different volume ratios. Considering that the proportion of C_{10}-DNTT in the mixed solution is much greater than that of F_4-TCNQ, it reaches its critical supersaturation level before the F_4-TCNQ molecules do during solvent evaporation. Therefore, during the solution-shearing process for the growth of F_4-TCNQ-loaded C_{10}-DNTT film, C_{10}-DNTT starts its crystal nucleation and growth earlier than the F_4-TCNQ molecules, and the F_4-TCNQ molecules are excluded from the growing C_{10}-DNTT crystals. Therefore, the dopant F_4-TCNQ molecules are most probably distributed on the surface of the C_{10}-DNTT layer. The optical microscopy (OM) and atomic force microscopy (AFM) images of the 10% F_4-TCNQ/C_{10}-DNTT films are shown in Figure 1c,d, wherein the films exhibited high uniformity over a millimeter scale and an atomic flatness with a root-mean-square of 3.2 Å. The film thickness was ∼3.8 nm, which is equivalent to that of pristine C_{10}-DNTT films, indicating that the F_4-TCNQ-loaded C_{10}-DNTT crystals adopt a similar molecular orientation to that of C_{10}-DNTT, wherein the molecules are aligned almost perpendicular to the SiO_2 substrate. Such structure promotes the realization of high-mobility devices because the dominant charge transport direction, *i.e.*, the intermolecular $\pi-\pi$ stacking, is parallel to the SiO_2 substrate.[27] Raman spectroscopy revealed characteristic peaks of C_{10}-DNTT in samples of 10% F_4-TCNQ/C_{10}-DNTT films across different regions and thicknesses, identical to those measured in the pristine C_{10}-DNTT films (Figure S2). The absence of distinct Raman peaks for F_4-TCNQ molecules indicates that, as low as their loading level was, the molecules were well-dispersed across the C_{10}-DNTT layer without any aggregate formation.

The chemical composition was characterized using transmission electron microscopy (TEM) coupled with energy-dispersive X-ray spectroscopy (EDS). TEM image of a typical sample of the 10% F_4-TCNQ/C_{10}-DNTT showing uniform morphology and its corresponding EDS spectrum are shown in Figure 1e,f. The fluorine and sulfur signals could be easily distinguished from each other on the EDS spectrum, and the atomic fraction of the fluorine was about 10% of the sum of the fluorine and sulfur atoms in the F_4-TCNQ/C_{10}-DNTT films (Figure 1f), and the molecular ratio of F_4-TCNQ is about 5.3%. X-ray photoelectron spectroscopy (XPS) was used to further characterize the surface chemical state, with survey and narrow scans of S 2*p*, and F 1*s* spectra of pristine C_{10}-DNTT, F_4-TCNQ, and F_4-TCNQ-loaded C_{10}-DNTT as shown in Figures S3 and 1g,h, respectively. For S 2*p* spectra of C_{10}-DNTT, the fitted peaks at approximately 163.63 ($2p_{3/2}$) and 164.83 ($2p_{1/2}$) eV correspond to S−C. In F_4-TCNQ/C_{10}-DNTT films, the peaks that correspond to S−C positively shift compared with those of the pristine C_{10}-DNTT, and the binding energies are increased to 163.71 and 164.93 eV, respectively. The F 1*s* peak was only detected in the F_4-TCNQ-loaded samples, confirming the presence of F_4-TCNQ molecules in the C_{10}-DNTT layer. We also compared the F 1*s* peak positions between the pristine F_4-TCNQ and F_4-TCNQ-loaded C_{10}-DNTT films. And the binding energy of F 1*s* in F_4-TCNQ/C_{10}-DNTT is decreased to 687.83 eV compared with the pristine F_4-TCNQ (687.99 eV). When F_4-TCNQ molecules are doped on the surface of the monolayer C_{10}-DNTT, the electrons are transferred from C_{10}-DNTT to F_4-TCNQ, leading to F_4-TCNQ anion and the increase of hole

https://doi.org/10.1021/acsnano.5c04783
ACS Nano 2025, 19, 16175−16187

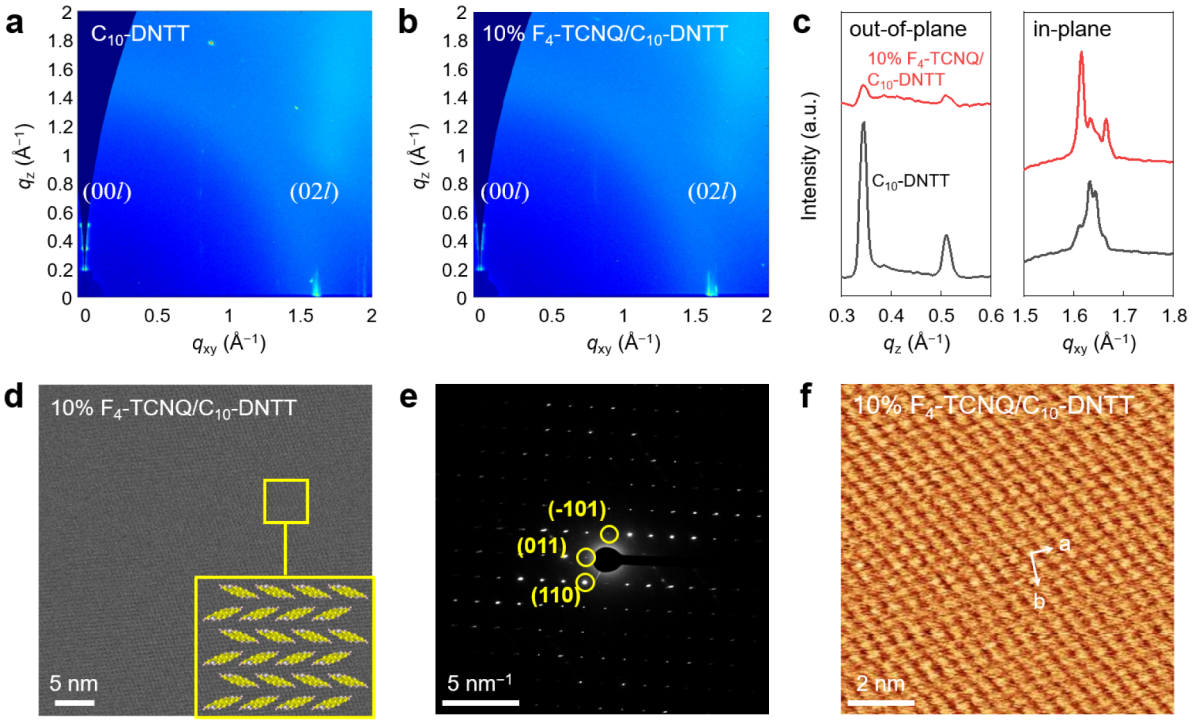

Figure 2. Crystallinity of 10% F_4-TCNQ/C_{10}-DNTT monolayer film. (a,b) The 2D GIWAXS patterns for pristine C_{10}-DNTT and 10% F_4-TCNQ/C_{10}-DNTT films, and (c) corresponding 1D plots of the GIWAXS patterns. (d) The high-resolution TEM image of 10% F_4-TCNQ/C_{10}-DNTT films and corresponding (e) selected-area electron diffraction patterns. (f) The high-resolution AFM image of 10% F_4-TCNQ/C_{10}-DNTT films.

concentration within the C_{10}-DNTT. Thus, the binding energy of S 2*p* moves toward higher binding energy, and the binding energy of F 1*s* moves toward lower binding energy, which provides direct evidence of charge transfer between the C_{10}-DNTT and F_4-TCNQ molecules. Therefore, we may conclude that the F_4-TCNQ-loaded monolayer C_{10}-DNTT films prepared using our straightforward one-step solution-shearing codeposition method is an effective structural analogue to the pristine C_{10}-DNTT films.

To gain insights into the potential impact of F_4-TCNQ molecules on the packing and orientation of C_{10}-DNTT molecules, the grazing-incidence wide-angle X-ray scattering (GIWAXS) was performed for both the 10% F_4-TCNQ-loaded monolayer C_{10}-DNTT and pristine multilayered C_{10}-DNTT reference samples (Figure 2a,b). For the pristine multilayer C_{10}-DNTT film, discernible (00*l*) reflections along the out-of-plane direction were observed, suggesting a lamellar layer-by-layer growth behavior. The (02*l*) reflections along the in-plane direction originated from the intermolecular π-π stacking,[28,29] indicating that the C_{10}-DNTT molecules are prone to adopt the edge-on orientation with respect to the SiO_2 substrate. Even for the monolayer-thick F_4-TCNQ-sensitized C_{10}-DNTT films, a sharp in-plane scattering pattern can be observed, indicating high quality of the self-assembled monolayer with good in-plane crystallinity.[30] The introduction of small amounts of F_4-TCNQ sensitizer into the C_{10}-DNTT solution facilitates efficient dopant anion generation through charge transfer.[31] Then, electrostatic repulsion between F_4-TCNQ anions mitigates aggregation, minimizing interference with C_{10}-DNTT crystallization and enabling the formation of F_4-TCNQ-loaded monolayer C_{10}-DNTT with long-range molecular ordering. Theoretically, due to the dissatisfaction with the Bragg diffraction condition for monolayer organic crystals, no scattering pattern should be observable in the out-of-plane direction;[32] nevertheless, a very weak out-of-plane peak was found in our sample due to minor imperfections (*i.e.*, isolated multilayer regions). The π-π *d*-spacing and lamellar *d*-spacing were extracted from the corresponding one-dimensional (1D) plot shown in Figure 2c. The lamellar *d*-spacing remained consistent, while the π-π *d*-spacing of the F_4-TCNQ-loaded sample increased slightly from 3.85 to 3.90 Å compared with the pristine sample (Table S1). Although tighter π-π stacking is beneficial for high-performance electrical conduction, its impact is minimal considering the 1.3% expansion of the π-π stacking.[16] Furthermore, the crystallinity and molecular structure were characterized by high-resolution TEM, and the F_4-TCNQ-loaded C_{10}-DNTT films are highly ordered with typical herringbone molecular packing (Figures 2d, S4).[33] The corresponding selected-area electron diffraction (SAED) with clear diffraction patterns is shown in Figure 2e, indicating the highly crystalline nature of the F_4-TCNQ-loaded C_{10}-DNTT films. And the molecular packing motif was further corroborated by the high-resolution AFM in Figure 2f. Furthermore, to intuitively demonstrate the impact of molecular sensitizer loading on the electrical properties of C_{10}-DNTT films, field-effect transistor (FET) devices with bottom-gate bottom-contact configuration were fabricated with the pristine and sensitized C_{10}-DNTT films to compare their electrical performance (Figure S5). The average carrier mobilities of the pristine and 10% F_4-TCNQ-loaded C_{10}-DNTT are 15.6 and 12.5 $cm^2\ V^{-1}\ s^{-1}$, respectively. Despite the slightly lower carrier mobility of the sensitized C_{10}-DNTT compared to the pristine C_{10}-DNTT, it still demonstrated excellent electrical performance, contributing to its high sensitivity toward gas analytes.

https://doi.org/10.1021/acsnano.5c04783
ACS Nano 2025, 19, 16175−16187

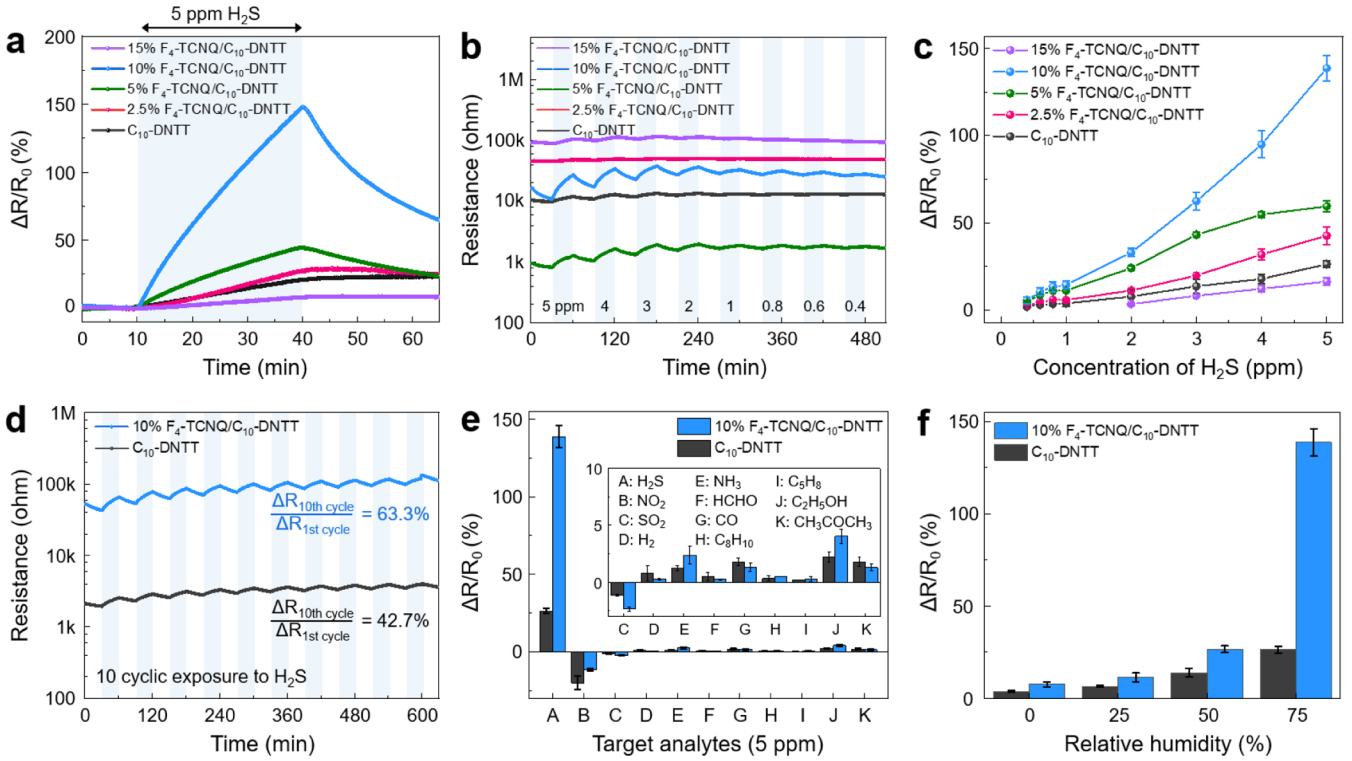

Figure 3. Gas sensing performance of pristine C_{10}-DNTT and F_4-TCNQ/C_{10}-DNTT monolayer-based gas sensors. (a) Response and recovery kinetics of pristine C_{10}-DNTT and F_4-TCNQ/C_{10}-DNTT monolayer with different loading ratios. (b) Resistance profiles for 5−0.4 ppm of H_2S, and (c) comparative gas response plots for pristine C_{10}-DNTT and F_4-TCNQ/C_{10}-DNTT-based sensors. (d) 10 cyclic tests for 5 ppm of H_2S of pristine C_{10}-DNTT and 10% F_4-TCNQ/C_{10}-DNTT-based sensors. (e) Selectivity tests for pristine C_{10}-DNTT and 10% F_4-TCNQ/C_{10}-DNTT toward 10 interfering gas analytes. (f) Gas sensing comparison chart of pristine C_{10}-DNTT and 10% F_4-TCNQ/C_{10}-DNTT-based sensors for 5 ppm of H_2S under different relative humidity conditions.

The chemiresistive gas sensors were fabricated to investigate the sensitizing effect of F_4-TCNQ molecules on the monolayer C_{10}-DNTT sensing layer for detecting hydrogen sulfide (H_2S), a toxic gas that poses significant risks to human health and industrial production.[34] F_4-TCNQ/C_{10}-DNTT films were used as the sensing materials, and the sensors were fabricated on patterned substrates using the solution-shearing method. Their sensing responses were monitored and characterized by a custom-built sensor setup under a nitrogen atmosphere.[35] It is hypothesized that at the monolayer thickness limit, the physical and chemical properties of the C_{10}-DNTT film surface can be effectively modulated by introducing F_4-TCNQ sensitizer molecules, which possess strong electron-withdrawing properties due to the high electronegativity of their fluorine atoms.[36] To explore this, the sensing capabilities of pristine monolayer C_{10}-DNTT films and those loaded with varying F_4-TCNQ concentrations (2.5%, 5%, 10%, and 15%) were evaluated for sensor optimization. The tests were conducted with 5 ppm of H_2S under 75% relative humidity (RH) and at room temperature. In organic semiconductor-based gas sensors, conductivity changes in the sensing layer are generally attributed to the surface charge transfer between the gas analytes and the sensing material.[37] Highly polar H_2S gas molecules can be adsorbed onto the sensor surface through dipole−dipole interaction, donating electrons to the sensing layer. This charge transfer process results in the annihilation of holes in the p-type C_{10}-DNTT semiconductor sensor, reducing its conductivity.[38] As shown in Figure 3a, the dynamic gas sensing results indicate that as the F_4-TCNQ loading ratio increased from 2.5% to 10%, the gas sensing response ((ΔR/R_0) × 100%, where ΔR is the resistance change after exposure to the gas analyte, and R_0 is the stabilized baseline resistance) also increased. In particular, the 10% F_4-TCNQ/C_{10}-DNTT monolayer sensor exhibited the highest sensing response of 138.7% among the five sensors tested, which is approximately 5.3-fold higher than that of the pristine C_{10}-DNTT sensor (26.4%). In contrast, the 2.5% and 5% F_4-TCNQ-loaded sensors showed lower responses of 42.8% and 59.6%, respectively. Increasing the loading ratio to 15% reduced sensing response by 16.4%, which was even lower than that of the pristine C_{10}-DNTT sensor. This decline is attributed to the decreased electrical conductivity caused by the dendritic growth of the C_{10}-DNTT films at high sensitizer concentrations (Figure S6). These results suggest that a small amount of F_4-TCNQ is insufficient to significantly enhance the surface reactivity of the monolayer C_{10}-DNTT sensing layer, while an excessive sensitizer loading disrupts film crystallization, leading to dramatic degradation of sensing performance. The significantly enhanced sensing response of the optimal 10% F_4-TCNQ/C_{10}-DNTT sensor can be attributed to the strong electron-withdrawing nature of F_4-TCNQ molecules that enhances the binding affinity for H_2S molecules, providing strong adsorption sites and maximizing the modulation of the surface electronic properties of the monolayer C_{10}-DNTT semiconductor. When compared to unsubstituted TCNQ-loaded C_{10}-DNTT-based sensors (Figure S7), the 10% TCNQ/C_{10}-DNTT sensor exhibited a sensing response of 52.1%, which remained lower than that of its F_4-TCNQ counterpart, particularly due to differences in charge transfer efficiency.[39,40] The fluorine atoms in F_4-TCNQ significantly

https://doi.org/10.1021/acsnano.5c04783
ACS Nano 2025, 19, 16175−16187

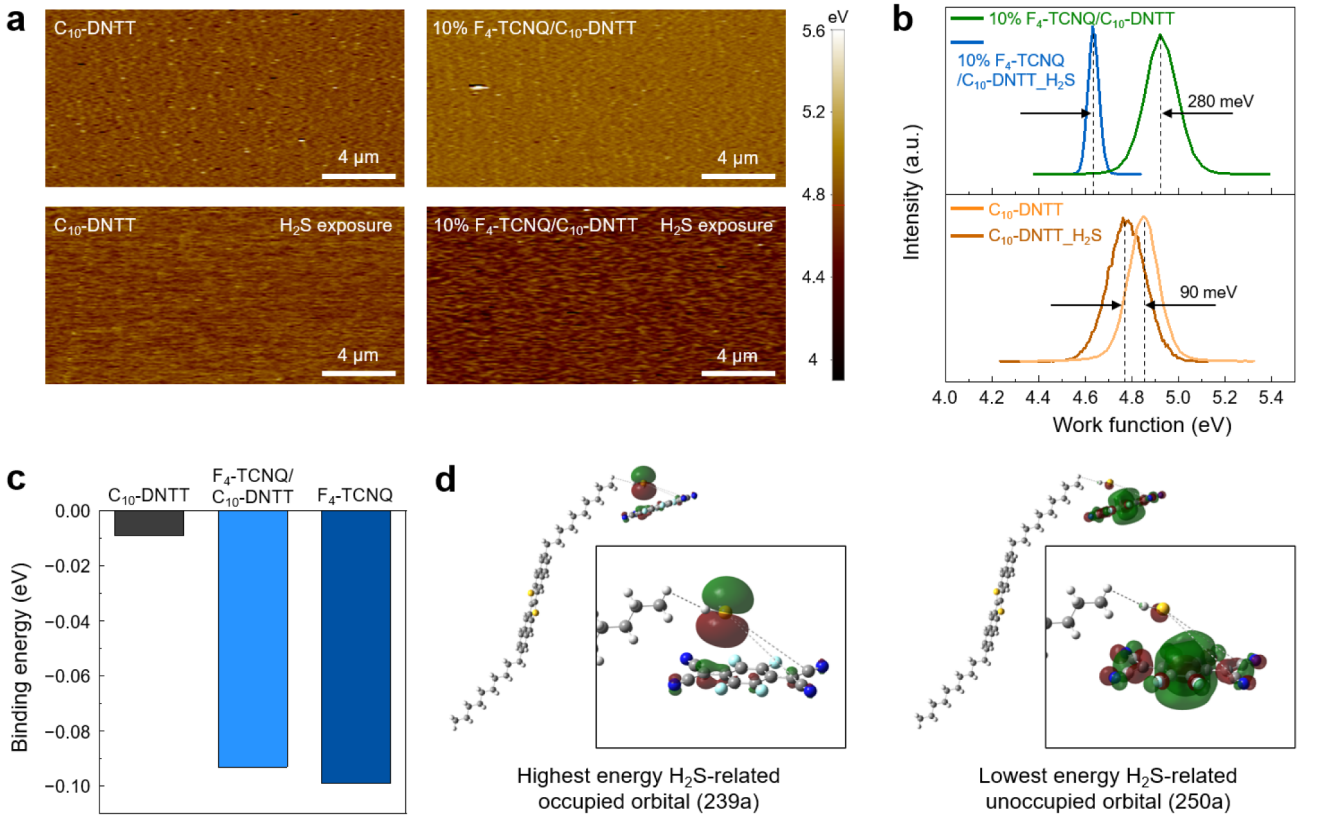

Figure 4. Investigation of work function and binding energy changes in pristine and F_4-TCNQ-loaded C_{10}-DNTT monolayers upon H_2S exposure. (a) KPFM work function map images for pristine C_{10}-DNTT and 10% F_4-TCNQ/C_{10}-DNTT monolayer and its corresponding work function maps after H_2S exposure and (b) work function distribution diagram extracted from the KPFM work function maps. (c) Binding energy of H_2S gas with C_{10}-DNTT, F_4-TCNQ/C_{10}-DNTT, and F_4-TCNQ. (d) Visualization of the highest-energy H_2S-related occupied orbital (239a) and the lowest-energy H_2S-related unoccupied orbital (250a).

strengthen its electron-withdrawing capability, leading to greater charge redistribution upon H_2S adsorption and thereby enhancing the sensor response. The solution-sheared F_4-TCNQ exhibited dendritic growth, hindering the formation of a uniform and continuous conductive film, which resulted in resistance exceeding the measurement limit (Figure S8). Given these structural limitations, F_4-TCNQ was instead leveraged as a sensitizer to enhance the H_2S sensing performance of C_{10}-DNTT by facilitating electronic interactions at the gas/semiconductor interface. These findings emphasize the crucial role of sensitizer selection in optimizing organic semiconductor-based gas sensors, with F_4-TCNQ demonstrating its effectiveness as a sensitizer for achieving enhanced gas sensing performance.

To further investigate the dynamic sensing behavior of F_4-TCNQ/C_{10}-DNTT, additional experiments were conducted with H_2S concentrations ranging from 0.4 to 5 ppm (Figures 3b,c, S9). Test results show that the sensing response to H_2S consistently increased with higher F_4-TCNQ loading ratios, from 2.5% to 10%, over the entire gas concentration range, demonstrating the effective sensitization effect of F_4-TCNQ molecules on the surface of monolayer C_{10}-DNTT films. The linearity of the response versus gas concentration from 0.4 to 5 ppm indicates reliable detection of H_2S within this range. Importantly, the 10% F_4-TCNQ/C_{10}-DNTT-based sensors demonstrated relatively stable response/recovery behavior over 10 cyclic exposures to 5 ppm of H_2S, retaining 63.3% of their initial response compared to 42.7% for the pristine C_{10}-DNTT sensor, indicating improved recovery characteristics and cyclability under repeated gas exposures (Figures 3d and S10). Note that incomplete recovery is a common characteristic of room-temperature gas sensors originating from the sluggish desorption of the target analyte. We further conducted long-term storage stability tests to evaluate the durability of the sensor. As shown in Figure S11, the 10% F_4-TCNQ/C_{10}-DNTT sensor maintained a consistent response to 5 ppm of H_2S, with an average value of 116.5 ± 25.7%, exhibiting only minor fluctuations when measured every 2 days over an 8-day period, demonstrating stable sensing performance over this period. Altogether, the observed enhancements in the sensing properties can be attributed to the well-defined molecular arrangement of the monolayer, which facilitates efficient charge transport, and the strong electron-withdrawing properties of the F_4-TCNQ sensitizer.

In addition to its high sensitivity and cyclic stability to H_2S, selectivity is a crucial factor for ensuring the practical viability of gas sensors. However, research on improving selectivity in organic semiconductor gas sensors is still lacking, as it depends on complex factors such as redox properties, electron transfer, and molecular interactions. Additionally, no studies have been reported on functionalizing sensitizers to enhance the selectivity for specific target gases. To investigate the effect of F_4-TCNQ as the molecular sensitizer, the selectivity of the sensors was evaluated against various interfering gas analytes. The 10% F_4-TCNQ/C_{10}-DNTT-based sensor exhibited excellent H_2S selectivity over other gases, including nitrogen dioxide (NO_2), sulfur dioxide (SO_2), hydrogen (H_2), ammonia (NH_3), formaldehyde (HCHO), carbon monoxide (CO), *p*-

https://doi.org/10.1021/acsnano.5c04783
ACS Nano 2025, 19, 16175−16187

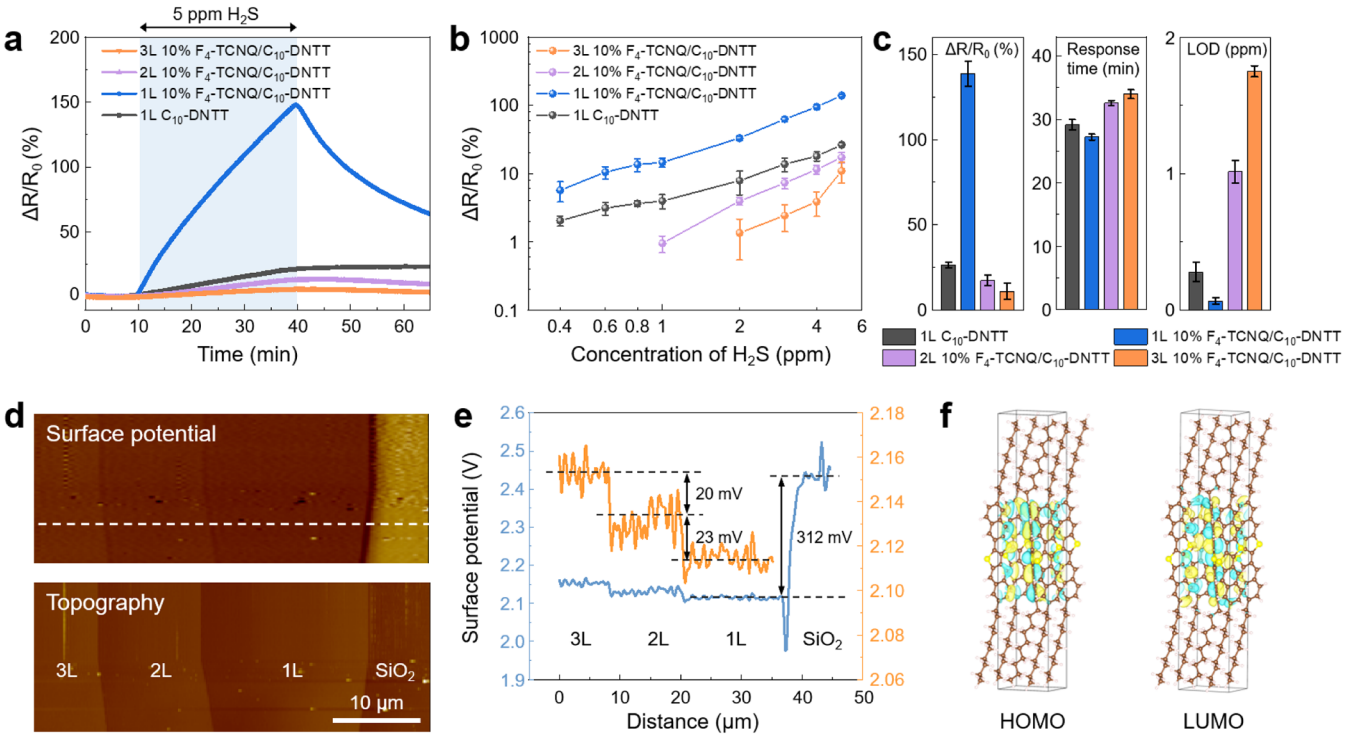

Figure 5. Molecular layer-number-dependent gas sensing characteristics. (a) Response and recovery kinetics, and (b) comparative gas response plots for 1L C_{10}-DNTT, 1L, 2L, and 3L F_4-TCNQ/C_{10}-DNTT-based sensors. (c) Molecular layer-number-dependent response, response time to 5 ppm of H_2S, and detection limit (bar chart). (d) KPFM topography and its corresponding surface potential map for multilayered 10% F_4-TCNQ/C_{10}-DNTT with step and terrace structure, and (e) the corresponding relative surface potential values of the cross-section indicated by the white dashed line in the surface potential distribution map. (f) The electronic distribution of HOMO and LUMO for the C_{10}-DNTT.

xylene (C_8H_{10}), isoprene (C_5H_8), ethanol (C_2H_5OH), and acetone (CH_3COCH_3), with its response to H_2S being an order of magnitude higher than that to the other gases (Figure 3e). On the contrary, the pristine C_{10}-DNTT-based sensor could not reliably distinguish the H_2S response from those of the interfering gases. These findings underscore the crucial role of the F_4-TCNQ sensitizer in enhancing H_2S selectivity, which is primarily governed by specific electronic interactions between the analyte gases and the F_4-TCNQ molecules (Figure S12).

Additionally, as H_2S is a biomarker for respiratory disorders such as halitosis and chronic obstructive pulmonary disease,[41] a sensor's capability for the sensitive and selective detection of H_2S even in high humidity conditions such as in exhaled breath is of utmost importance. As such, the sensing response of pristine and 10% F_4-TCNQ/C_{10}-DNTT sensors to 5 ppm of H_2S was systematically evaluated at different humidity levels (0, 25, 50, 75% RH) (Figure 3f). Both sensors exhibited an increased response with rising humidity, with the 10% F_4-TCNQ/C_{10}-DNTT sensor showing a notable improvement in highly humid conditions (75% RH), achieving a response 3-fold higher than that of the pristine sensor. This observation highlights the significant influence of water molecules on H_2S sensing, with humidity-assisted improvements in sensing performance closely aligned with previously reported findings.[37,42−44] Especially the rapid increase in H_2S response at high humidity (75% RH) can be attributed to the percolation threshold of the hydration layer, where increased H_2S dissolution and ionization lead to a higher concentration of reactive species. Additionally, the high electron affinity of the F_4-TCNQ sensitizer facilitates charge redistribution through hydrogen bonding interactions with H_2O molecules, thereby enhancing charge transport in C_{10}-DNTT. Further experiments confirmed that while 10% F_4-TCNQ/C_{10}-DNTT-based sensors exhibit minor resistance variations with humidity changes, their response is primarily governed by H_2S exposure (Figure S13).

The chemiresistive gas sensing measurements revealed that the F_4-TCNQ-loaded monolayer C_{10}-DNTT sensors exhibited enhanced sensitivity and selectivity toward the H_2S analytes, showing comparable performance to previously reported organic material-based H_2S sensors (Table S2).[45−54] To elucidate the F_4-TCNQ sensitization effects during the gas sensing process, Kelvin probe force microscopy (KPFM) was utilized to investigate the work function changes following F_4-TCNQ loading and H_2S exposure, respectively (Figure S14). Highly oriented pyrolytic graphite (HOPG) and thermally evaporated Au film served as calibration reference samples for determining the work function (Figures S15 and 16). Figure 4a,b presents the work function mapping images and the corresponding distribution diagram, showing that the average work function of pristine and F_4-TCNQ-loaded C_{10}-DNTT films is 4.85 and 4.92 eV, respectively. The observed downward shift of the work function by 70 meV toward the highest occupied molecular orbital (HOMO) confirms the electronic sensitization effect of the F_4-TCNQ molecule,[55] aligning with the results obtained from ultraviolet photoelectron spectroscopy (UPS) (Figure S17). Furthermore, a noticeable brightness-darkening change in the work function mapping images was observed upon H_2S exposure, indicating a direct electron transfer process and n-type "doping" (*i.e.*, charge injection) induced by H_2S molecules.[56] The work

https://doi.org/10.1021/acsnano.5c04783
ACS Nano 2025, 19, 16175−16187

function of F_4-TCNQ-loaded C_{10}-DNTT decreased by 280 meV due to H_2S exposure, which is over 3 times higher than that of the pristine C_{10}-DNTT, indicating the powerful sensitizing effect of F_4-TCNQ in the gas sensing mechanism. These findings further support the increased resistance observed in the chemiresistive sensing measurements of both pristine and 10% F_4-TCNQ/C_{10}-DNTT sensors to H_2S.

To fundamentally elucidate the mechanisms behind the enhanced H_2S sensing capabilities in F_4-TCNQ/C_{10}-DNTT as observed experimentally, density functional theory (DFT) calculations were conducted to examine the binding energies between H_2S and various system components. Figure 4c presents the binding energies of H_2S with the C_{10}-DNTT and F_4-TCNQ components. The F_4-TCNQ/C_{10}-DNTT system shows a binding energy approximately ten times higher than that of C_{10}-DNTT alone, closely mirroring the binding energy between F_4-TCNQ and H_2S. These results highlight minimal interaction between H_2S and C_{10}-DNTT, likely due to the alkyl chains in C_{10}-DNTT, which do not support strong interactions with polar molecules like H_2S. The binding energy increase in the F_4-TCNQ/C_{10}-DNTT system suggests that F_4-TCNQ is responsible for significantly enhancing the interaction with H_2S. Due to its strong electron-withdrawing properties, F_4-TCNQ exhibits a polar nature, raising the binding affinity for H_2S molecules. This enhancement is comparable to the binding energy between F_4-TCNQ and H_2S alone, confirming F_4-TCNQ as the dominant interacting factor within the composite system. Molecular orbital analysis, shown in Figures 4d and S18, identified that both the highest energy H_2S-related occupied orbitals and the lowest energy H_2S-related unoccupied orbitals involve F_4-TCNQ rather than C_{10}-DNTT. This finding suggests that H_2S primarily interacts electronically with F_4-TCNQ, indicating strong electronic coupling crucial for effective sensing, as it can impact the charge transport properties of semiconductor films upon gas binding.

Generally, the electrical performance of few-layer organic crystals is comparable to that of their bulk counterparts due to their 2D nature, efficient charge carrier injection, and high surface-to-volume ratio.[15,57] Then, layer-dependent gas sensing responses were characterized to investigate the critical role of the monolayer structure in achieving high sensitivity to gas analytes. After first determining that a 10% loading ratio for F_4-TCNQ was optimal based on the sensing performance, we subsequently evaluated the 10% F_4-TCNQ/C_{10}-DNTT-based sensors with varying C_{10}-DNTT layer numbers prepared by adjusting the solution-shearing growth temperature. Figure 5a shows the dynamic sensing performance of pristine monolayer C_{10}-DNTT and 10% F_4-TCNQ/C_{10}-DNTT sensors with varying layer numbers: monolayer (1L), bilayer (2L), and trilayer (3L). Upon exposure to 5 ppm of H_2S, the 1L 10% F_4-TCNQ/C_{10}-DNTT sensor showed the highest response, almost 8.1-fold higher than the 2L sensor and 12.7-fold higher than the 3L sensor. Interestingly, the response of the pristine 1L C_{10}-DNTT sensor was even greater than that of the 2L and 3L F_4-TCNQ-sensitized sensors, emphasizing the critical importance of maintaining a monolayer structure for optimal organic sensing performance. Furthermore, upon dynamic exposure to H_2S concentrations ranging from 0.4 to 5 ppm (Figure 5b), the 1L 10% F_4-TCNQ/C_{10}-DNTT sensor exhibited the highest sensing response across the entire concentration range, attributed to the direct interactions between the charge carriers of monolayer films and H_2S molecules. The sensing response, response time, and limit of detection (LOD) were extracted and summarized in Figure 5c. The pristine C_{10}-DNTT sensor exhibited a response of 26.4%, a response time of 29.2 min, and an LOD of 0.28 ppm. As the number of layers of F_4-TCNQ/C_{10}-DNTT increased from 1L to 2L and 3L, the sensing response dramatically decreased from 138.7% to 17.2% and 10.9%, respectively. The response time increased from 27.2 min for 1L to 32.6 min for 2L and 34.0 min for 3L, while the LOD values were measured at 0.07, 1.02, and 1.75 ppm, respectively. Furthermore, the overall gas sensing performance of the pristine 1L C_{10}-DNTT sensor exceeded that of the F_4-TCNQ-sensitized multilayer sensors (2L and 3L), emphasizing the critical importance of a monolayer sensing layer for achieving high-performance organic chemical sensors.

Considering the effectiveness of layer-dependent gas sensing characteristics in molecular sensitizer-loaded multilayer C_{10}-DNTT sensors, we further explored the charge carrier behaviors to reveal the sensing mechanism. The KPFM was first used to map the surface potential and topography of the F_4-TCNQ-loaded multilayer C_{10}-DNTT films, which exhibited a step-and-terrace structure. Figure 5d presents the surface potential and corresponding topography images, highlighting the difference in surface potential between the F_4-TCNQ-sensitized C_{10}-DNTT film region and the SiO_2 substrate attributed to the different work functions of these materials. In the sensitized C_{10}-DNTT film region, the distinct molecular layers were easily identifiable in the topography images, with a height difference of 3.8 nm, indicating that molecular layers beyond the 1L maintain similar molecular packing and orientation. The surface potential image reveals slight color contrasts among the 1L, 2L, and 3L layers, reflecting the difference in surface potential between the adjacent molecular layers. As shown in Figure 5e, the relative surface potential difference (Δ_{SP}) between the 1L layer and the SiO_2 substrate is approximately 312 mV, and the Δ_{SP} between 1L and 2L is about 23 mV, which slightly decreases to 20 mV between the 2L and 3L layers. Notably, when the number of C_{10}-DNTT layers is increased to and above four, the color contrast in the surface potential becomes negligible for additional layers (Figure S19), indicating that the charge carriers are mainly confined to the first few molecular layers at the semiconductor/dielectric interface, where the built-in field is most potent. From the perspective of C_{10}-DNTT molecules, the conducting π-core region of the C_{10}-DNTT molecule is spatially separated by insulating alkyl chains (Figure 5f), allowing the formation of a continuously extended density of states only within a single layer. Consequently, the multilayer C_{10}-DNTT films exhibited discrete carrier distribution rather than a continuous distribution, with carrier density decreasing quadratically with distance from the semiconductor/dielectric interface.[58,59] Therefore, the layer-dependent gas sensing results can be attributed to the different carrier distributions in the multilayer C_{10}-DNTT films, whereby interactions between carriers and gas molecules are most pronounced in the first monolayer. The monolayer films, characterized by a high surface-to-volume ratio, reduced the diffusion length of gas molecules and confined surface charge transfer and charge transport channels to a localized region, enhancing sensitivity to gas analytes. Additionally, the highly ordered nature of monolayer C_{10}-DNTT films promoted the adsorption and desorption of gas analytes, improving overall gas sensing rates and recovery characteristics. As the thickness increased to 2L

https://doi.org/10.1021/acsnano.5c04783
ACS Nano 2025, 19, 16175−16187

and 3L, the surface adsorption and slower diffusion of H_2S into the interfacial layer impeded direct interactions with charge carriers, resulting in diminished sensing capabilities.[60] These results demonstrate the potential of highly crystalline monolayer C_{10}-DNTT for developing sensitive and selective chemical gas sensors while elucidating the sensitizing effect of the F_4-TCNQ molecules, suggesting that this promising strategy for sensor design may be extended to other monolayer organic semiconductor films with compatible electronic properties and molecular structures.

CONCLUSION

In this study, we developed high-performance H_2S gas sensors using molecular sensitizer-loaded monolayer organic semiconductors fabricated through a straightforward solution-shearing codeposition method. The monolayer thickness and the grain boundary-free surface of the F_4-TCNQ sensitizer-loaded monolayer C_{10}-DNTT effectively eliminate the gas diffusion bottleneck and facilitate direct interactions between the H_2S gas and the monolayer C_{10}-DNTT. This design confines the charge transport and transfer process of H_2S within the same conducting π-core channel of the sensing layer. Taking advantage of the sensitization effects of the F_4-TCNQ, the F_4-TCNQ/C_{10}-DNTT sensors exhibited a response that was 5.3-fold higher than that of the pristine C_{10}-DNTT sensor, along with high selectivity and device stability. Furthermore, we elucidated that the few-layer structure of the sensitized organic semiconductors provides an optimal platform for investigating novel physical phenomena and advancing high-performance sensing applications.

EXPERIMENTAL SECTION

Materials. The C_{10}-DNTT powder (sublimed >99%) was purchased from Luminescence Technology Corp., and the TCNQ (>99.0%), F_4-TCNQ (>98.0%), and anisole (>99.0%) were purchased from Tokyo Chemical Industry (TCI). Trichloro(octadecyl)silane (OTS, >90%), and chloroform (anhydrous, ≥99%) were purchased from Sigma-Aldrich. All chemicals were received and utilized without further purification.

Preparation of F_4-TCNQ-Loaded Monolayer C_{10}-DNTT Films. The highly doped p^{++} SiO_2 substrates with a 300 nm thermal oxide layer were used for the organic film deposition. The SiO_2 substrate underwent ultrasonic cleaning in acetone, isopropanol, and deionized water for 10 min each, followed by UV-ozone treatment for 20 min to make the substrate surface hydrophilic, which is advantageous for the solution-processed ultrathin organic films. C_{10}-DNTT was dissolved in anisole at 0.2 mg/mL and sonicated for 20 min to enhance dissolution. The resulting C_{10}-DNTT solution was heated at 85 °C for about 4 h before use. Similarly, F_4-TCNQ was dissolved in anisole at 0.2 mg/mL and placed under ambient conditions. The mixed solution consisted of C_{10}-DNTT and F_4-TCNQ solutions with different volume ratios (2.5%, 5%, 10%, and 15%). For the preparation of the OTS-treated glass blade, the glass was immersed in a 3 wt % OTS chloroform solution for about 12 h, followed by rinsing with chloroform, acetone, and isopropanol. The OTS-treated glass blade, with its hydrophobic surface, was used to improve the crystallinity during the organic film deposition. Pristine and F_4-TCNQ-loaded C_{10}-DNTT films were deposited using a home-built solution-shearing setup with a hot plate on the sample stage. During the solution-shearing coating process, the speed and temperature are the main factors that affect the film layer morphology. The slower speed is preferred to reduce the deposition temperature and minimize the thermal cracks of the organic semiconductor film, thereby achieving high electrical performance devices (Figures S20 and S21). Here, the shearing speed of 10 μm/s is applied since the minimum deposition rate of our home-made solution-shearing setup is 10 μm/s. A 20 μL volume of organic solution was injected into the gap between the blade and substrate with the shearing speed of 0.01 mm/s using the linear translation stage, with a gap of 100 μm and a tilt angle of 15° between the blade and substrate. The growth temperature for 1L 10% F_4-TCNQ/C_{10}-DNTT film was maintained at around 60 °C, and the growth temperature for 2L and 3L 10% F_4-TCNQ/C_{10}-DNTT films are 65 and 69 °C, respectively. For the preparation of TCNQ-loaded monolayer C_{10}-DNTT films, the same fabrication method was applied, with F_4-TCNQ replaced by TCNQ in the solution preparation step.

Materials Characterizations. The OM images were taken from an OLYMPUS optical microscopy (BX53M). The regular AFM and KPFM measurements were performed using the Park NX10 AFM system, and the gold-coated AFM tip (NSC36/Cr−Au) was used for the electrical sideband mode KPFM measurements. The ZYA grade HOPG was used to calibrate the work function. The F_4-TCNQ-loaded C_{10}-DNTT films were deposited onto the SiO_2 substrates and fixed on a metal plate using a silver paste to enable sample biasing during KPFM measurements. High-resolution AFM was conducted using the Cypher AFM system. The pristine and F_4-TCNQ-loaded monolayer C_{10}-DNTT films were directly deposited on the copper grid for TEM-EDS measurements (200 kV Multi EDS Field Emission TEM, Talos F200X G2). High-resolution TEM and SAED patterns were obtained using a Cryo Field Emission TEM (300 kV, Krios G4, Thermo Fisher). XPS and UPS were conducted using in situ X-ray photoelectron spectroscopy (AXIS SUPRA model (Kratos)). For XPS measurements, an Al Kα X-ray source was employed to characterize the surface chemical states, while UPS measurements, using a He I (21.2 eV) UV source with an energy step size of 0.025 eV, were used to determine the work function of pristine C_{10}-DNTT and 10% F_4-TCNQ/C_{10}-DNTT films. The work function was calculated by subtracting the onset of secondary electron cutoff energy from the UV source energy (21.2 eV). GIWAXS experiments were performed at the 9 Å beamline of the Pohang Accelerator Laboratory.

Electrical and Gas Sensing Measurements. For FET device fabrication, a 90 nm highly doped p^{++} SiO_2 substrate was used. The FET devices were characterized under ambient conditions using a probe station and a Keithley 4200A-SCS parameter analyzer. The carrier mobility was extracted in the saturation region of the FET device using the equation: $I_{DS} = \left(\frac{WC_i}{2L}\right)\mu_{FET}(V_G - V_{Th})^2$, where L and W are the channel length and width, respectively, C_i is the gate dielectric capacitance, V_{Th} is the threshold voltage. For gas sensor fabrication, IDE consisting of a 5 nm Cr adhesion layer and a 30 nm Au with a width of 100 μm and a gap of 50 μm were deposited on the SiO_2 substrate using e-beam evaporation. C_{10}-DNTT and F_4-TCNQ-loaded C_{10}-DNTT with different loading ratios were directly deposited onto the sensor substrates with patterned electrodes. Platinum wires were then attached to the electrode pads using the silver paste to form electrical contacts. The resistance of the gas sensors was

https://doi.org/10.1021/acsnano.5c04783
ACS Nano 2025, 19, 16175−16187

measured using a custom-built testing system comprising a 16-channel multiplexer (34972A, Agilent), solenoid valves, and mass flow controllers (MFC). Before gas exposure, all sensors were equilibrated under ambient conditions for 12 h. Gas exposure followed a 30 min on/off cycle. To control the humidity of the reference gas, part of the gas stream was passed through a water bubbler maintained at 37 °C, and then this humidified gas was mixed with the balance gas using the MFC. All gas sensor tests were conducted at room temperature without applying additional voltage to the sensor substrate. Response times were defined as the time required for the sensor resistance to reach 90% of its maximum response ($(R - R_{min})/R_{max} \geq 0.9$). Data analysis involved calculating the resistance ratio $(\Delta R/R_0) \times 100\%$, where ΔR represents the change in resistance upon exposure to the gas analyte, and R_0 is the stabilized baseline resistance. This ratio served as an indicator of the sensitivity to the target gas, providing a quantitative indication of the response to gas exposure. Sensing measurements were performed on more than three independent sensors, with error bars calculated from the obtained values.

Density Functional Theory Calculations and Binding Energy Optimization. DFT calculations were conducted using the Gaussian16 software package.[61] The calculations employed the accurate description of van der Waals complexes by density functional theory, including empirical corrections with the 6-31G(d) basis set. Geometric optimization was conducted through the quadratic convergence (QC) method to ensure stable convergence, followed by self-consistent field (SCF) calculation with tight convergence criteria to determine energy and orbital properties. To ensure accuracy, the maximum SCF cycle was set to 1024. Three random initial configurations were chosen for each system, and the configuration yielding the lowest binding energy was selected for further analysis.

ASSOCIATED CONTENT

Supporting Information

The Supporting Information is available free of charge at https://pubs.acs.org/doi/10.1021/acsnano.5c04783.

The OM, AFM, and SAED characterizations for the pristine monolayer C_{10}-DNTT films; Raman spectroscopy, XPS, and UPS spectra of the 10% F_4-TCNQ/C_{10}-DNTT films; the schematic diagram of the molecular packing of C_{10}-DNTT molecules; the electrical performance of the pristine and 10% F_4-TCNQ-loaded C_{10}-DNTT field-effect transistors; the AFM morphological images of 15% F_4-TCNQ/C_{10}-DNTT; response traces of TCNQ/C_{10}-DNTT monolayers with different loading ratios; optical microscopy images of pristine F_4-TCNQ and its resistance profile; the dynamic gas sensing result of the 10% F_4-TCNQ/C_{10}-DNTT-based chemiresistive sensors; the cyclic tests for 5 ppm of H_2S of pristine C_{10}-DNTT and F_4-TCNQ-loaded C_{10}-DNTT sensors with different loading ratios; long-term stability results of 10% F_4-TCNQ/C_{10}-DNTT-based sensors; resistance profiles for SO_2 of pristine C_{10}-DNTT and 10% F_4-TCNQ/C_{10}-DNTT-based sensors; resistance traces of 10% F_4-TCNQ/C_{10}-DNTT-based sensors at 25%, 50%, and 75% RH; the layer morphology of the F_4-TCNQ/C_{10}-DNTT under different shearing speeds and deposition temperatures and their FET electrical performance; the KPFM device structure; the KPFM work function map of the HOPG and Au reference samples and the KPFM surface potential map of the multilayered 10% F_4-TCNQ/C_{10}-DNTT; DFT optimized configuration of F_4-TCNQ/C_{10}-DNTT system toward H_2S; the π-π d-spacing and lamella d-spacing extracted from the 1D GIWAXS plot; summary of sensing properties for organic material-based H_2S sensors operating at room temperature (PDF)

AUTHOR INFORMATION

Corresponding Authors

Jihan Kim − *Department of Chemical and Biomolecular Engineering, Korea Advanced Institute of Science and Technology (KAIST), Daejeon 34141, Republic of Korea;* orcid.org/0000-0002-3844-8789; Email: jihankim@kaist.ac.kr

Yun Li − *National Laboratory of Solid-State Microstructures, School of Electronic Science and Engineering, Collaborative Innovation Center of Advanced Microstructures, Nanjing University, Nanjing 210093, P. R. China;* orcid.org/0000-0003-1753-7317; Email: yli@nju.edu.cn

Il-Doo Kim − *Department of Materials Science and Engineering, Korea Advanced Institute of Science and Technology (KAIST), Daejeon 34141, Republic of Korea;* orcid.org/0000-0002-9970-2218; Email: idkim@kaist.ac.kr

Kibum Kang − *Department of Materials Science and Engineering, Korea Advanced Institute of Science and Technology (KAIST), Daejeon 34141, Republic of Korea; Graduate School of Semiconductor Technology, Korea Advanced Institute of Science and Technology (KAIST), Daejeon 34141, Republic of Korea;* orcid.org/0000-0003-1674-1826; Email: kibumkang@kaist.ac.kr

Authors

Jianhang Guo − *National Laboratory of Solid-State Microstructures, School of Electronic Science and Engineering, Collaborative Innovation Center of Advanced Microstructures, Nanjing University, Nanjing 210093, P. R. China; Department of Materials Science and Engineering, Korea Advanced Institute of Science and Technology (KAIST), Daejeon 34141, Republic of Korea*

Jong Won Baek − *Department of Materials Science and Engineering, Korea Advanced Institute of Science and Technology (KAIST), Daejeon 34141, Republic of Korea*

Yeonghun Kang − *Department of Chemical and Biomolecular Engineering, Korea Advanced Institute of Science and Technology (KAIST), Daejeon 34141, Republic of Korea;* orcid.org/0000-0001-5191-5735

Dongyoung Kim − *Graduate School of Semiconductor Technology, Korea Advanced Institute of Science and Technology (KAIST), Daejeon 34141, Republic of Korea*

Chungseong Park − *Department of Materials Science and Engineering, Korea Advanced Institute of Science and Technology (KAIST), Daejeon 34141, Republic of Korea*

Junhee Woo − *Department of Materials Science and Engineering, Korea Advanced Institute of Science and Technology (KAIST), Daejeon 34141, Republic of Korea*

Taoyu Zou − *Department of Chemical Engineering, Pohang University of Science and Technology (POSTECH), Pohang 37673, Republic of Korea*

https://doi.org/10.1021/acsnano.5c04783
ACS Nano 2025, 19, 16175−16187

Euichul Shin − *Department of Materials Science and Engineering, Korea Advanced Institute of Science and Technology (KAIST), Daejeon 34141, Republic of Korea*
Qijing Wang − *School of Integrated Circuits, Nanjing University, Suzhou 215163, P. R. China;* orcid.org/0000-0003-0115-5330
Yong-Young Noh − *Department of Chemical Engineering, Pohang University of Science and Technology (POSTECH), Pohang 37673, Republic of Korea;* orcid.org/0000-0001-7222-2401
Steve Park − *Department of Materials Science and Engineering, Korea Advanced Institute of Science and Technology (KAIST), Daejeon 34141, Republic of Korea*

Complete contact information is available at: https://pubs.acs.org/10.1021/acsnano.5c04783

Author Contributions

[▽]J.G., J.W.B, Y.K., and D.K. contributed equally to this work.

Notes

The authors declare no competing financial interest.

ACKNOWLEDGMENTS

This work was supported by National Key Research and Development Program of China (Grant Nos. 2022YFA1203802 and 2021YFA0715600), National Natural Science Foundation of China (Grant No. 62374081), the National Research Foundation of Korea grant funded by the Korea government, Ministry of Science and ICT (Development of Nanofiber Yarn Based Compound Sensor as a Comprehensive Wearable Healthcare Solution) (Grant No. RS-2024-00357296). Y.H.K. and J.H.K. acknowledged funding from the National Research Foundation of Korea (NRF) under Project Number RS-2024-00435493. Q.J.W. acknowledged funding from the Natural Science Foundation of Jiangsu Province (BK20230779) and the National Natural Science Foundation of China (Grant No. 62404095). J.H.G. acknowledged the financial support from the China Scholarship Council (No.202106190148).

REFERENCES

(1) Zhang, X.; Dong, H.; Hu, W. Organic Semiconductor Single Crystals for Electronics and Photonics. *Adv. Mater.* **2018**, *30* (44), 1801048.
(2) Zhang, Q.; Li, M.; Li, L.; Geng, D.; Chen, W.; Hu, W. Recent Progress in Emerging Two-Dimensional Organic−Inorganic van Der Waals Heterojunctions. *Chem. Soc. Rev.* **2024**, *53*, 3096−3133.
(3) Zhang, Y.; Wang, Y.; Gao, C.; Ni, Z.; Zhang, X.; Hu, W.; Dong, H. Recent Advances in N-Type and Ambipolar Organic Semiconductors and Their Multi-Functional Applications. *Chem. Soc. Rev.* **2023**, *52*, 1331−1381.
(4) Yu, C.; He, J.; Cheng, X.; Lin, H.; Yu, H.; Lu, J. An Ion-In-Conjugation-Boosted Organic Semiconductor Gas Sensor Operating at High Temperature and Immune to Moisture. *Angew. Chem., Int. Ed.* **2021**, *60*, 15328−15334.
(5) Lu, J.; Liu, D.; Zhou, J.; Chu, Y.; Chen, Y.; Wu, X.; Huang, J. Porous Organic Field-Effect Transistors for Enhanced Chemical Sensing Performances. *Adv. Funct. Mater.* **2017**, *27* (20), 1700018.
(6) Kang, B.; Jang, M.; Chung, Y.; Kim, H.; Kwak, S. K.; Oh, J. H.; Cho, K. Enhancing 2D Growth of Organic Semiconductor Thin Films with Macroporous Structures via a Small-Molecule Heterointerface. *Nat. Commun.* **2014**, *5*, 4752.
(7) Lu, J.; Wang, Z.; Xue, D.; Chu, M.; Zhang, Y.; Ji, L.; Wang, Q.; Jiang, X.; Sun, Y.; Miao, Q.; Dong, B.; Huang, L.; Chi, L. Organic Heteroepitaxy Growth of High-Performance Responsive Thin Films with Solution Shearing Crystals as Templates. *ACS Mater. Lett.* **2022**, *4*, 1314−1321.
(8) Yin, Y.; Wang, X.; Xue, D.; Lu, J.; Zhang, Y.; Gong, W.; Yan, C.; Wang, Z.; Wang, L.; Chi, L.; Huang, L. Bulk Trapping Organic Semiconductor with Amino-Additive Enabling Ultrasensitive NO_2 Sensors. *ACS Appl. Mater. Interfaces* **2024**, *16*, 23684−23694.
(9) Wang, Z.; Hu, J.; Lu, J.; Zhu, X.; Zhou, X.; Huang, L.; Chi, L. Charge Transport Manipulation via Interface Doping: Achieving Ultrasensitive Organic Semiconductor Gas Sensors. *ACS Appl. Mater. Interfaces* **2023**, *15*, 8355−8366.
(10) Chen, H.; Zhang, W.; Li, M.; He, G.; Guo, X. Interface Engineering in Organic Field-Effect Transistors: Principles, Applications, and Perspectives. *Chem. Rev.* **2020**, *120*, 2879−2949.
(11) Xiao, M.; Liu, J.; Liu, C.; Han, G.; Shi, Y.; Li, C.; Zhang, X.; Hu, Y.; Liu, Z.; Gao, X. Sub-5 nm single crystalline organic p−n heterojunctions. *Nat. Commun.* **2021**, *12* (1), 2774.
(12) Zeng, J.; He, D.; Qiao, J.; Li, Y.; Sun, L.; Li, W.; Xie, J.; Gao, S.; Pan, L.; Wang, P.; Xu, Y. Ultralow Contact Resistance in Organic Transistors via Orbital Hybridization. *Nat. Commun.* **2023**, *14* (1), 324.
(13) Jiang, L.; Dong, H.; Meng, Q.; Li, H.; He, M.; Wei, Z.; He, Y.; Hu, W. Millimeter-Sized Molecular Monolayer Two-Dimensional Crystals. *Adv. Mater.* **2011**, *23*, 2059−2063.
(14) Peng, B.; Cao, K.; Ho, A.; Lau, Y.; Chen, M.; Lu, Y.; Chan, P. K. L. Crystallized Monolayer Semiconductor for Ohmic Contact Resistance, High Intrinsic Gain, and High Current Density. *Adv. Mater.* **2020**, *32* (34), 2002281.
(15) Cao, M.; Zhang, C.; Cai, Z.; Xiao, C.; Chen, X.; Yi, K.; Yang, Y.; Lu, Y.; Wei, D. Enhanced Photoelectrical Response of Thermodynamically Epitaxial Organic Crystals at the Two-Dimensional Limit. *Nat. Commun.* **2019**, *10* (1), 756.
(16) Park, S. K.; Kim, J. H.; Park, S. Y. Organic 2D Optoelectronic Crystals: Charge Transport, Emerging Functions, and Their Design Perspective. *Adv. Mater.* **2018**, *30* (42), 1704759.
(17) Li, H.; Shi, Y.; Han, G.; Liu, J.; Zhang, J.; Li, C.; Liu, J.; Yi, Y.; Li, T.; Gao, X.; Di, C.; Huang, J.; Che, Y.; Wang, D.; Hu, W.; Liu, Y.; Jiang, L. Monolayer Two-dimensional Molecular Crystals for an Ultrasensitive OFET-based Chemical Sensor. *Angew. Chem., Int. Ed.* **2020**, *59*, 4380−4384.
(18) Qiu, F.; Liu, J.; Zhang, H.; Li, H.; Liu, J.; Shi, X.; Li, C.; Shi, Y.; Hu, Y.; Guo, Y.; Gao, X.; Ai, S.; Jiang, L. Flexible Monolayer Molecular Crystal-Field Effect Transistors for Ultrasensitive and Selective Detection of Dimethoate. *Adv. Electron. Mater.* **2020**, *6* (11), 2000579.
(19) Chen, H.; Dong, S.; Bai, M.; Cheng, N.; Wang, H.; Li, M.; Du, H.; Hu, S.; Yang, Y.; Yang, T.; Zhang, F.; Gu, L.; Meng, S.; Hou, S.; Guo, X. Solution-Processable, Low-Voltage, and High-Performance Monolayer Field-Effect Transistors with Aqueous Stability and High Sensitivity. *Adv. Mater.* **2015**, *27*, 2113−2120.
(20) Jiang, S.; Wang, Q.; Qian, J.; Guo, J.; Duan, Y.; Wang, H.; Shi, Y.; Li, Y. Molecular Layer-Defined Transition of Carrier Distribution and Correlation with Transport in Organic Crystalline Semiconductors. *ACS Appl. Mater. Interfaces* **2020**, *12*, 26267−26275.
(21) Guo, J.; Jiang, S.; Pei, M.; Xiao, Y.; Zhang, B.; Wang, Q.; Zhu, Y.; Wang, H.; Jie, J.; Wang, X.; Shi, Y.; Li, Y. Few-Layer Organic Crystalline van Der Waals Heterojunctions for Ultrafast UV Phototransistors. *Adv. Electron. Mater.* **2020**, *6* (6), 2000062.
(22) Zhang, F.; Di, C.; Berdunov, N.; Hu, Y.; Hu, Y.; Gao, X.; Meng, Q.; Sirringhaus, H.; Zhu, D. Ultrathin Film Organic Transistors: Precise Control of Semiconductor Thickness via Spin-Coating. *Adv. Mater.* **2013**, *25*, 1401−1407.
(23) Peng, B.; Huang, S.; Zhou, Z.; Chan, P. K. L. Solution-Processed Monolayer Organic Crystals for High-Performance Field-Effect Transistors and Ultrasensitive Gas Sensors. *Adv. Funct. Mater.* **2017**, *27* (29), 1700999.
(24) Giri, G.; Verploegen, E.; Mannsfeld, S. C. B.; Atahan-Evrenk, S.; Kim, D. H.; Lee, S. Y.; Becerril, H. A.; Aspuru-Guzik, A.; Toney, M. F.; Bao, Z. Tuning Charge Transport in Solution-Sheared Organic Semiconductors Using Lattice Strain. *Nature* **2011**, *480*, 504−508.

(25) Kang, M. J.; Doi, I.; Mori, H.; Miyazaki, E.; Takimiya, K.; Ikeda, M.; Kuwabara, H. Alkylated Dinaphtho[2,3-b: 2′,3′- f]Thieno[3,2-b]Thiophenes (C_n-DNTTs): Organic Semiconductors for High-Performance Thin-Film Transistors. *Adv. Mater.* **2011**, *23*, 1222−1225.
(26) Scaccabarozzi, A. D.; Basu, A.; Aniés, F.; Liu, J.; Zapata-Arteaga, O.; Warren, R.; Firdaus, Y.; Nugraha, M. I.; Lin, Y.; Campoy-Quiles, M.; Koch, N.; Müller, C.; Tsetseris, L.; Heeney, M.; Anthopoulos, T. D. Doping Approaches for Organic Semiconductors. *Chem. Rev.* **2022**, *122*, 4420−4492.
(27) Yang, J.; Yan, D.; Jones, T. S. Molecular Template Growth and Its Applications in Organic Electronics and Optoelectronics. *Chem. Rev.* **2015**, *115*, 5570−5603.
(28) Wang, Q.; Juarez-Perez, E. J.; Jiang, S.; Xiao, M.; Qian, J.; Shin, E.-Y.; Noh, Y.-Y.; Qi, Y.; Shi, Y.; Li, Y. Approaching Isotropic Transfer Integrals in Crystalline Organic Semiconductors. *Phys. Rev. Mater.* **2020**, *4*, 044604.
(29) Liu, D.; Zhang, Y.; Li, G. Nanomorphology in A−D−A Type Small Molecular Acceptors-Based Bulk Heterojunction Polymer Solar Cells. *J. Energy Chem.* **2019**, *35*, 104−123.
(30) Shi, Y.; Jiang, L.; Liu, J.; Tu, Z.; Hu, Y.; Wu, Q.; Yi, Y.; Gann, E.; McNeill, C. R.; Li, H.; Hu, W.; Zhu, D.; Sirringhaus, H. Bottom-up Growth of n-Type Monolayer Molecular Crystals on Polymeric Substrate for Optoelectronic Device Applications. *Nat. Commun.* **2018**, *9* (1), 2933.
(31) Mun, J.; Kang, J.; Zheng, Y.; Luo, S.; Wu, Y.; Gong, H.; Lai, J.-C.; Wu, H.-C.; Xue, G.; Tok, J. B.-H.; Bao, Z. F_4-TCNQ as an Additive to Impart Stretchable Semiconductors with High Mobility and Stability. *Adv. Electron. Mater.* **2020**, *6* (6), 2000251.
(32) Zhou, Z.; Wu, Q.; Wang, S.; Huang, Y.-T.; Guo, H.; Feng, S.-P.; Chan, P. K. L. Field-Effect Transistors Based on 2D Organic Semiconductors Developed by a Hybrid Deposition Method. *Adv. Sci.* **2019**, *6* (19), 1900775.
(33) He, D.; Zhang, Y.; Wu, Q.; Xu, R.; Nan, H.; Liu, J.; Yao, J.; Wang, Z.; Yuan, S.; Li, Y.; Shi, Y.; Wang, J.; Ni, Z.; He, L.; Miao, F.; Song, F.; Xu, H.; Watanabe, K.; Taniguchi, T.; Xu, J.-B.; Wang, X. Two-Dimensional Quasi-Freestanding Molecular Crystals for High-Performance Organic Field-Effect Transistors. *Nat. Commun.* **2014**, *5*, 5162.
(34) Ali, F. I. M.; Awwad, F.; Greish, Y. E.; Mahmoud, S. T. Hydrogen Sulfide (H_2S) Gas Sensor: A Review. *IEEE Sens. J.* **2019**, *19*, 2394−2407.
(35) Baek, J. W.; Han, S.; Lee, S. E.; Ahn, J.; Park, C.; Nam, J. S.; Kim, Y. H.; Shin, E.; Kim, M.; Jang, J.-S.; Kim, J.; Park, H. J.; Kim, I.-D. Cobalt-Doped Ceria Sensitizer Effects on Metal Oxide Nanofibers: Heightened Surface Reactivity for High-Performing Chemiresistive Sensors. *ACS Nano* **2024**, *18*, 19568−19580.
(36) Zhang, Y.; Qiao, J.; Gao, S.; Hu, F.; He, D.; Wu, B.; Yang, Z.; Xu, B.; Li, Y.; Shi, Y.; Ji, W.; Wang, P.; Wang, X.; Xiao, M.; Xu, H.; Xu, J.-B.; Wang, X. Probing Carrier Transport and Structure-Property Relationship of Highly Ordered Organic Semiconductors at the Two-Dimensional Limit. *Phys. Rev. Lett.* **2016**, *116*, 016602.
(37) He, J.; Liang, B.; Yan, X.; Liu, F.; Wang, J.; Yang, Z.; You, R.; Wang, C.; Sun, P.; Yan, X.; Lin, H.; Kang, B.; Wang, Y.; Lu, G. A TPA-DCPP Organic Semiconductor Film-Based Room Temperature NH_3 Sensor for Insight into the Sensing Properties. *Sens. Actuators, B* **2021**, *327*, 128940.
(38) Dai, J.; Ogbeide, O.; Macadam, N.; Sun, Q.; Yu, W.; Li, Y.; Su, B.-L.; Hasan, T.; Huang, X.; Huang, W. Printed Gas Sensors. *Chem. Soc. Rev.* **2020**, *49*, 1756−1789.
(39) Ramanathan, R.; Martin, L. L.; Bond, A. M.; Bansal, V. Emerging Applications of TCNQ-Based Metal−Organic Semiconducting Materials. *ACS Appl. Nano Mater.* **2024**, *7*, 28057−28073.
(40) Vo, N. T.; Bond, A. M.; Martin, L. L. Systematic and Non-Systematic Substituent Effects Gleaned from Studies on CuTCNQF_n (n = 0, 1, 2, 4): Electrocrystallisation and Characterisation of CuTCNQF. *Inorg. Chim. Acta* **2020**, *505*, 119458.
(41) Suzuki, Y.; Saito, J.; Munakata, M.; Shibata, Y. Hydrogen Sulfide as a Novel Biomarker of Asthma and Chronic Obstructive Pulmonary Disease. *Allergol. Int.* **2021**, *70*, 181−189.
(42) Kanaparthi, S.; Singh, S. G. Solvent-Free Fabrication of a Room Temperature Ammonia Gas Sensor by Frictional Deposition of a Conducting Polymer on Paper. *Org. Electron.* **2019**, *68*, 108−112.
(43) Cha, J.-H.; Kim, D.-H.; Park, C.; Choi, S.-J.; Jang, J.-S.; Yang, S. Y.; Kim, I.-D.; Choi, S.-Y. Low-Thermal-Budget Doping of 2D Materials in Ambient Air Exemplified by Synthesis of Boron-Doped Reduced Graphene Oxide. *Adv. Sci.* **2020**, *7* (7), 1903318.
(44) Rath, R. J.; Talebian, S.; Giaretta, J.; Naficy, S.; Dehghani, F. Organic-Based Chemiresistive Sensors for Detection of Water-Soluble Gases: Strategies and Roadmap for Enhancing Sensing Performance. *Adv. Funct. Mater.* **2025**, *35* (11), 2417323.
(45) Deng, Y.; Zhao, M.; Ma, Y.; Liu, S.; Liu, M.; Shen, B.; Li, R.; Ding, H.; Cheng, H.; Sheng, X.; Fu, W.; Li, Z.; Zhang, M.; Yin, L. A Flexible and Biomimetic Olfactory Synapse with Gasotransmitter-Mediated Plasticity. *Adv. Funct. Mater.* **2023**, *33* (18), 2214139.
(46) Zhao, X.; Tong, Y.; Tang, Q.; Tian, H.; Liu, Y. Highly Sensitive H_2S Sensors Based on Ultrathin Organic Single-Crystal Microplate Transistors. *Org. Electron.* **2016**, *32*, 94−99.
(47) Sharma, M.; Patel, C.; Sriram, S.; Mukherjee, S.; Das, A. K. Investigating the Role of Amide to Thioamide Substitution of a Covalent Organic Polymer for the Selective Chemodetection of H_2S at Room Temperature. *ACS Appl. Polym. Mater.* **2023**, *5*, 10065−10072.
(48) Cao, Z.; Huo, X.; Ma, Q.; Song, J.; Pan, Q.; Chen, L.; Lai, J.; Shan, X.; Gao, J. TFT-CN/P3HT Blending Active Layer Based Two-Component Organic Field-Effect Transistor for Improved H_2S Gas Detection. *Sens. Actuators, B* **2023**, *385*, 133685.
(49) Mehrolia, M. S.; Kumar, D.; Verma, A.; Singh, A. K. Fabrication and Characterization of Self-Assembled Low Voltage Operated OTFT for H_2S Gas Sensor for Oil and Gas Industry. *IEEE Trans. Electron Devices* **2024**, *71*, 769−776.
(50) Trul, A. A.; Chekusova, V. P.; Polinskaya, M. S.; Kiselev, A. N.; Agina, E. V.; Ponomarenko, S. A. NH_3 and H_2S Real-Time Detection in the Humid Air by Two-Layer Langmuir-Schaefer OFETs. *Sens. Actuators, B* **2020**, *321*, 128609.
(51) Yuvaraja, S.; Bhyranalyar, V. N.; Bhat, S. A.; Surya, S. G.; Yelamaggad, C. V.; Salama, K. N. A Highly Selective Electron Affinity Facilitated H_2S Sensor: The Marriage of Tris(Keto-Hydrazone) and an Organic Field-Effect Transistor. *Mater. Horiz.* **2021**, *8*, 525−537.
(52) Li, L.; Zhang, S.; Lu, Y.; Zhang, J.; Zhang, X.; Wang, R.; Huang, J. Highly Selective and Sensitive Detection of Volatile Sulfur Compounds by Ionically Conductive Metal-Organic Frameworks. *Adv. Mater.* **2021**, *33* (52), 2104120.
(53) Yang, Y.; Liu, Z.; Chen, L.; Yao, J.; Lin, G.; Zhang, X.; Zhang, G.; Zhang, D. Conjugated Semiconducting Polymer with Thymine Groups in the Side Chains: Charge Mobility Enhancement and Application for Selective Field-Effect Transistor Sensors toward CO and H_2S. *Chem. Mater.* **2019**, *31*, 1800−1807.
(54) Li, X.; Jiang, Y.; Xie, G.; Tai, H.; Sun, P.; Zhang, B. Copper Phthalocyanine Thin Film Transistors for Hydrogen Sulfide Detection. *Sens. Actuators, B* **2013**, *176*, 1191−1196.
(55) Pei, K.; Lau, A. H. Y.; Chan, P. K. L. Understanding Molecular Surface Doping of Large Bandgap Organic Semiconductors and Overcoming the Contact/Access Resistance in Organic Field-Effect Transistors. *Phys. Chem. Chem. Phys.* **2020**, *22*, 7100−7109.
(56) Bisht, P.; Belle, B. D.; Aggarwal, P.; Ghosh, A.; Xing, W.; Kaur, N.; Singh, J. P.; Mehta, B. R. Gas Sensing Properties of PLD Grown 2D SnS Film: Effect of Film Thickness, Metal Nanoparticle Decoration, and In Situ KPFM Investigation. *Small* **2024**, *20* (23), 2307037.
(57) Yang, F.; Cheng, S.; Zhang, X.; Ren, X.; Li, R.; Dong, H.; Hu, W. 2D Organic Materials for Optoelectronic Applications. *Adv. Mater.* **2018**, *30* (2), 1702415.
(58) Brondijk, J. J.; Roelofs, W. S. C.; Mathijssen, S. G. J.; Shehu, A.; Cramer, T.; Biscarini, F.; Blom, P. W. M.; De Leeuw, D. M. Two-

Dimensional Charge Transport in Disordered Organic Semiconductors. *Phys. Rev. Lett.* **2012**, *109*, 056601.
(59) Jiang, S.; Qian, J.; Wang, Q.; Duan, Y.; Guo, J.; Zhang, B.; Sun, H.; Wang, X.; Liu, C.; Shi, Y.; Li, Y. Probing Coulomb Interactions on Charge Transport in Few-Layer Organic Crystalline Semiconductors by the Gated van Der Pauw Method. *Adv. Electron. Mater.* **2020**, *6* (7), 2000136.
(60) Wang, Z.; Huang, L.; Zhu, X.; Zhou, X.; Chi, L. An Ultrasensitive Organic Semiconductor NO_2 Sensor Based on Crystalline TIPS-Pentacene Films. *Adv. Mater.* **2017**, *29* (38), 1703192.
(61) Frisch, M. J.; Trucks, G. W.; Schlegel, H. B.; Scuseria, G. E.; Robb, M. A.; Cheeseman, J. R.; Scalmani, G.; Barone, V.; Petersson, G. A.; Nakatsuji, H., *Gaussian 16, Revision A.03*; Gaussian, Inc.: Wallingford, CT, 2016.

https://doi.org/10.1021/acsnano.5c04783
ACS Nano 2025, 19, 16175−16187